

## DISCOVERY OF RAPIDLY MOVING PARTIAL X-RAY ABSORBERS WITHIN $\gamma$ CASSIOPEIAE

K. HAMAGUCHI<sup>1,2</sup>, L. OSKINOVA<sup>3</sup>, C. M. P. RUSSELL<sup>4</sup>, R. PETRE<sup>4</sup>, T. ENOTO<sup>5,6</sup>, K. MORIHANA<sup>7</sup>, M. ISHIDA<sup>8</sup>

<sup>1</sup>CRESST and X-ray Astrophysics Laboratory NASA/GSFC, Greenbelt, MD 20771, USA, Kenji.Hamaguchi@nasa.gov

<sup>2</sup>Department of Physics, University of Maryland, Baltimore County, 1000 Hilltop Circle, Baltimore, MD 21250, USA

<sup>3</sup>Institute of Physics and Astronomy, University of Potsdam, 14476 Potsdam, Germany

<sup>4</sup>X-ray Astrophysics Laboratory NASA/GSFC, Greenbelt, MD 20771, USA

<sup>5</sup>The Hakubi Center for Advanced Research, Kyoto University, Kyoto 606-8302, Japan

<sup>6</sup>Department of Astronomy, Kyoto University, Kitashirakawa- Oiwake-cho, Sakyo-ku, Kyoto 606-8502, Japan

<sup>7</sup>Nishi-Harima Astronomical Observatory, Center for Astronomy, University of Hyogo, 407-2, Nichigaichi, Sayo-cho, Sayo, Hyogo, 670-5313, Japan

<sup>8</sup>The Institute of Space and Astronautical Science, Japan Aerospace Exploration Agency, 3-1-1 Yoshinodai, Chuo-ku, Sagamihara, 252-5210, Japan

### ABSTRACT

Gamma Cassiopeiae is an enigmatic Be star with unusually strong hard X-ray emission. The *Suzaku* observatory detected six rapid X-ray spectral hardening events called “softness dips” in a  $\sim 100$  ksec duration observation in 2011. All the softness dip events show symmetric softness ratio variations, and some of them have flat bottoms apparently due to saturation. The softness dip spectra are best described by either  $\sim 40\%$  or  $\sim 70\%$  partial covering absorption to  $kT \sim 12$  keV plasma emission by matter with a neutral hydrogen column density of  $\sim 2-8 \times 10^{21}$  cm<sup>-2</sup>, while the spectrum outside of these dips is almost free of absorption. This result suggests the presence of two distinct X-ray emitting spots in the  $\gamma$  Cas system, perhaps on a white dwarf companion with dipole mass accretion. The partial covering absorbers may be blobs in the Be stellar wind, the Be disk, or rotating around the white dwarf companion. Weak correlations of the softness ratios to the hard X-ray flux suggest the presence of stable plasmas at  $kT \sim 0.9$  and 5 keV, which may originate from the Be or white dwarf winds. The formation of a Be star and white dwarf binary system requires mass transfer between two stars;  $\gamma$  Cas may have experienced such activity in the past.

*Keywords:* stars: emission-line, Be — stars: individual ( $\gamma$  Cassiopeiae) — stars: winds, outflows — X-rays: stars — white dwarfs — blue stragglers

### 1. INTRODUCTION

The classical Be stars are enigmatic massive stars with circumstellar disks, whose formation is not yet understood (e.g. Rivinius et al. 2013). A subset of the class, the  $\gamma$  Cas analogues, is particularly interesting with unusually hard ( $kT \gtrsim 10$  keV), luminous ( $L_X \sim 10^{32}-10^{33}$  ergs s<sup>-1</sup>) X-ray activity compared with that of normal main-sequence B stars (see e.g. Smith et al. 2016). The origin of their high energy activity has been controversial for a long time.

As the name suggests,  $\gamma$  Cassiopeia ( $\gamma$  Cas) is the prototype of the  $\gamma$  Cas class. It is a B0.5 IVe star (Tokovinin 1997) with  $R_* \sim 10 R_\odot$  and  $L \sim 34000 L_\odot$  (e.g., Sigut & Jones 2007) at a distance of  $188 \pm 4$  pc (van Leeuwen 2007). Doppler measurements of optical emission lines suggest that  $\gamma$  Cas is a binary with a nearly circular orbit ( $e < 0.08$ ) at a period of 203.5 days (Nemravová et al. 2012; Smith et al. 2012). The primary stellar mass is estimated from its effective temperature at  $\approx 15 M_\odot$  (Harmanec et al. 2000), and the companion mass is estimated at  $\sim 0.8-1 M_\odot$  from the orbital solutions, assuming an orbital inclination of  $45^\circ$  (Nemravová et al. 2012; Smith et al. 2012). The Be disk has been resolved with optical/near-infrared interferometry. Its FWHM radius ranges between  $1.5-7.25 R_*$ , depending on the measured wavelength (see references in Rivinius et al. 2013). From elongation of the interferometric images, the disk inclination is estimated to be  $\approx 40-55^\circ$  (Stee et al. 2012; Gies et al. 2007).

Gamma Cas has been studied intensively in X-rays with almost all the available observatories (White et al. 1982; Murakami et al. 1986; Parmar et al. 1993; Kubo et al. 1998; Smith et al. 1998; Owens et al. 1999; Robinson & Smith 2000; Smith et al. 2004; Lopes de Oliveira et al. 2010; Smith et al. 2012; Shrader et al. 2015; Motch et al. 2015). In

all these observations the X-ray characteristics were found to be similar. The light curve is highly variable, with a slowly varying “basal” component on timescales of  $\sim 10$  ksec and a rapidly varying “shot” component on timescales of  $\sim 10$ – $100$  sec. Comparisons of the light curves in different energy bands have revealed strong variations in spectral hardness, which are apparently uncorrelated to these flux variations. The X-ray spectrum shows multiple emission lines, notably from hydrogen-like, helium-like and quasi-neutral  $K$  shell iron. Though these lines are apparently weak, the broad-band spectrum does not show any non-thermal signature in continuum up to 100 keV and can be formally reproduced with optically thin thermal emission from a  $kT \sim 14$  keV plasma with  $EM \approx 1\text{--}5 \times 10^{55} \text{ cm}^{-3}$  and small metal abundance at  $\sim 0.3$  solar, suffering absorption at  $\log N_{\text{H}} \sim 21\text{--}22 \text{ cm}^{-2}$  on average. Nitrogen and oxygen  $K$  shell lines and the iron  $L$  shell line complex, resolved with high resolution grating spectra, originates from a few relatively cool plasma components at  $kT \sim 0.1\text{--}4$  keV with  $EM$  of  $1\text{--}5 \times 10^{54} \text{ cm}^{-3}$ .

Because of its high energy emission, the presence of a degenerate companion, such as a neutron star or a white dwarf (WD), has been discussed. The X-ray properties — no signature of non-thermal emission, no pulsation, and moderate X-ray luminosity at  $\sim 10^{33} \text{ ergs s}^{-1}$  — argue against the neutron star hypothesis. The former two properties match with those of accreting WDs (cataclysmic variables), but the X-ray luminosity is around the upper end of such systems and might be too high for mass accretion onto the known  $\gamma$  Cas companion. As  $\gamma$  Cas has a circumstellar disk and shows apparently random, frequent X-ray shots, an alternative mechanism of a magnetic dynamo driven by the star-disk differential rotation has also been proposed. However, no strong magnetic field has been detected from  $\gamma$  Cas, nor has the validity of this mechanism been confirmed by theoretical investigations. [Smith et al. \(2016\)](#) discuss the pros and cons of these hypotheses in detail.

In this paper, we present our analysis of the color variation in the 0.3–10 keV X-ray band of  $\gamma$  Cas observed with the *Suzaku* X-ray observatory ([Mitsuda et al. 2007](#)) in 2011. This observation was originally aimed at measuring the detailed spectral shape of the X-ray emission above 15 keV. The initial result, combined with the archival *INTEGRAL* data, which suggests no power-law component in the  $\gamma$  Cas spectrum up to 100 keV, is summarized in [Shrader et al. \(2015\)](#). The long-elapsed observation also enables us to monitor the spectral softness variation in the soft band in detail and help discover that the variation, seen also in earlier observations, is caused by rapid changes of the line of sight absorption to the hard, variable X-ray emission.

## 2. OBSERVATION AND DATA ANALYSIS

*Suzaku* pointed at  $\gamma$  Cas for  $\sim 111$  ksec starting on 2011 July 13, 00<sup>h</sup> 06<sup>m</sup> in UT. During this observation, *Suzaku* used two instruments: the X-ray Imaging Spectrometer (XIS, [Koyama et al. 2007](#)) at the focal plane of the thin-foil X-Ray Telescope (XRT, [Serlemitsos et al. 2007](#)), and the Hard X-ray Detector (HXD, [Takahashi et al. 2007](#); [Kokubun et al. 2007](#)). In this paper, we focus on the XRT+XIS datasets. The XIS consists of four X-ray CCD cameras, XIS0–3, three of which (XIS0, 2 and 3) use front-illuminated (FI) CCD chips, while one (XIS1) uses a back-illuminated (BI) chip. The FI chips have good hard X-ray sensitivity, covering the X-ray band between 0.5–10 keV, while the BI chip has good soft X-ray sensitivity down to  $\sim 0.3$  keV. During this observation, the sensors XIS0, 1 and 3 were working. Gamma Cas was put at the XIS on-axis (XIS nominal) position and the XIS net exposures are each 55.4 ksec. The detailed observational set-up and the basic analysis procedure of this dataset can be found in [Shrader et al. \(2015\)](#). Throughout this paper, we use the analysis package HEASoft version 6.19 and *Suzaku* version 16 or later, and the CALDB versions, xis20110630 and xrt20110630, for the data calibration. We also use the *Xanadu* package for the timing (*xronos* version 5.22) and spectral (*xspect* version 12.9.0i, [Arnaud 1996](#)) analysis and assume the *aspl* solar abundance table ([Asplund et al. 2009](#))<sup>1</sup>. In the timing analysis, the time origin is defined at Modified Julian Date 55755.0.

## 3. RESULT

### 3.1. Light Curves and Softness Ratio Curves

We generate XIS light curves of  $\gamma$  Cas between 0.5–1 keV (count rate, CR[0.5–1]), 1–2 keV (CR[1–2]), 2–4 keV (CR[2–4]) and 4–9 keV (CR[4–9]) from the combined XIS (0, 1 and 3) data using the same procedure as described in Section 3.3 of [Shrader et al. \(2015\)](#) (Figure 1). All these light curves show intense fluctuations by  $\approx 50\%$  on timescales of  $\lesssim 1$  ksec, as also seen in earlier X-ray observations of  $\gamma$  Cas ([White et al. 1982](#); [Horaguchi et al. 1994](#); [Kubo et al. 1998](#); [Smith et al. 1998](#); [Lopes de Oliveira et al. 2010](#); [Smith et al. 2012](#)). During the observation, the fluxes in all energy bands gradually decline to reach the lowest level at  $\sim 100$  ksec from the observation start, stay at that level

<sup>1</sup> We also tried the *wilms* abundance table for the spectral fits (Section 3.3), but these two models give negligible ( $\lesssim 5\%$ ) differences in the best-fit spectral parameters except for the plasma elemental abundance, which is higher by  $\sim 30\%$  with the *wilms* abundance table.

for  $\sim 5$  ksec, and then recover abruptly to the original flux level. Such short, low flux intervals called ‘‘cessation’’ were also seen in earlier observations (Robinson & Smith 2000; Robinson et al. 2002; Smith et al. 2016).

In order to investigate the differences between these light curves, we produce softness ratio curves with respect to CR[4–9]. We define the softness ratios, SR[0.5–1], SR[1–2], and SR[2–4] as the divisions of CR[0.5–1], CR[1–2], and CR[2–4] by CR[4–9] (i.e. SR[band] = CR[band]/CR[4–9] where ‘‘band’’ is 0.5–1, 1–2, or 2–4). The resulting color variability plots are shown in Figure 2. SR[2–4] is flat, consistent with a constant model at above 97% confidence (reduced  $\chi^2 = 1.23$ , 134 degrees of freedom, hereafter dof). However, SR[1–2] begins to show dip-like structures; a constant model is inconsistent with this SR plot at a reduced  $\chi^2$  of 10.1 (134 dof). These dips are even more pronounced in the softest band SR[0.5–1], and a constant model is rejected with a reduced  $\chi^2$  of 25.0 (134 dof). Figure 2 also demonstrates that, in the softer energy band, these dips are deeper than the average SR value outside of these dips. Similar spectral color variations seen as spikes in the hardness ratio plots (CR[4.5–10]/CR[0.3–1]) were reported previously in *XMM-Newton* observations (Lopes de Oliveira et al. 2010; Smith et al. 2012).

The above result also implies that each SR variation has a baseline level at the highest clustering value ( $\sim 0.6$  for SR[0.5–1] and  $\sim 2.1$  for SR[1–2]). There are important reasons to choose this level as the baseline instead of a lower one. First, it constitutes a clear peak at  $\sim 2.1$  for SR[1–2] and a maximum at  $\sim 0.6$  for SR[0.5–1] (see histograms at the right panels of Figure 2). Second, all significant transitions of the SR value start or end at these baseline levels. For example, if we choose the baseline level at  $\sim 0.4$  in SR[0.5–1], transitions at  $\sim 65$  and 73 ksec just pass this level. This level does not seem to be important physically and/or phenomenologically. Third, our baseline levels are consistent with that of zero absorption to  $kT \sim 12$  keV X-ray emission, which is the major X-ray emission component of  $\gamma$  Cas (see section 3.3). We therefore believe our choice of the baseline levels is the most physically reasonable.

Such spectral hardening could be produced by plasma heating, but these softness dip events do not occur coincidentally with intrinsic flux increases traced with CR[4–9], which would indicate plasma heating (Figure 2). They can be, instead, produced by changes in the absorption column. The photo-electric absorption cross section depends on the X-ray photon energy as  $E^{-3}$  (Morrison & McCammon 1983). Cold matter in the line of sight with columns of  $N_{\text{H}} \sim 10^{21} - 10^{22} \text{ cm}^{-2}$  absorb only soft X-rays below  $\sim 2$  keV.

In SR[0.5–1], we identify six clear softness dips, two of which (dips 1 and 6) overlap with the start or end of the observation. Softness dips 1, 3, 4 and 6 show rapid fall and rise, while the others have relatively slow transitions. Softness dips 1, 4 and 6 have flat bottoms, while the others instantly transition from fall to rise. Though parts of these dips are missed because of the gaps in the data, their shapes appear to be symmetric. We therefore construct a phenomenological model, describing each softness dip by a symmetrical trapezoid with four parameters — center time ( $t_c$ ), flat bottom duration ( $T_{\text{fb}}$ ), fall/rise transition duration ( $T_{\text{tr}}$ ), and depth ( $SR_{\text{d}}$ ). Then, the shape of the softness dip  $i$  can be formulated as:

$$SR^i(t) = 0 \quad (T_{\text{fb}}^i/2 + T_{\text{tr}}^i < |t - t_c^i|) \quad (1)$$

$$= -\frac{(T_{\text{tr}}^i + T_{\text{fb}}^i/2 - |t - t_c^i|)}{T_{\text{tr}}^i} SR_{\text{d}}^i \quad (T_{\text{fb}}^i/2 < |t - t_c^i| \leq T_{\text{fb}}^i/2 + T_{\text{tr}}^i) \quad (2)$$

$$= -SR_{\text{d}}^i \quad (|t - t_c^i| \leq T_{\text{fb}}^i/2) \quad (3)$$

SR[0.5–1] can be described as the sum of the six softness dips on top of the baseline level ( $SR_{\text{bl}}$ ) as follows.

$$SR(t) = SR_{\text{bl}} + \sum_{i=1}^6 SR^i(t) \quad (4)$$

We fit this model to SR[0.5–1]. The best-fit result is shown in Figure 3 and Table 1.  $T_{\text{tr}}$  is roughly divided into short (0.4–1 ksec) and long (4–7 ksec) timescales.  $T_{\text{fb}}$  is distributed in a broad range from zero to  $>20$  ksec.

### 3.2. Stable Spectral Component

We further exploit the information in the SRs and find a weak but significant correlation between each SR and CR[4–9]; at each energy band, the SR is higher in lower CR[4–9] (Figure 4, upper panels). The same plot but only with data points outside of the softness dips (hereafter called the baseline interval:  $\sum [t_c^i + (T_{\text{fb}}^i/2 + T_{\text{tr}}^i), t_c^{i+1} - (T_{\text{fb}}^{i+1}/2 + T_{\text{tr}}^{i+1})]$ ) shows a linear correlation more clearly (see the black data points in the bottom panels of Figure 4). In fact, a linear fit to the SR[0.5–1] vs. CR[4–9] plot improves from 22.3 (dof: 133) to 2.45 (dof: 52) in reduced  $\chi^2$  value by excluding the softness dip data points. Therefore, this correlation probably is not produced by coincidental dip events. Such correlations can be produced if the plasma temperature tends to be higher or the absorption tends to be stronger at higher CR[4–9]. However, a similar plot for SR[15–40] in Figure 3 of Shrader et al. (2015) did not show

any dependence on CR[4–9], even though the temperature increase should be most clearly seen in the highest energy range. It is also difficult to imagine a straightforward physical mechanism that could produce stronger absorption in the higher CR[4–9] range.

We suggest here that this correlation is most consistently explained by soft, stable X-ray emission. The presence of relatively cool plasmas at  $kT \sim 0.1\text{--}4$  keV is suggested from nitrogen  $K$ , oxygen  $K$ , and iron  $L$  emission lines detected in high resolution grating spectra (Smith et al. 2004, 2012). If some or all of these components are present stably during the *Suzaku* observation, their emission should produce the observed SR and CR[4–9] relation. We derive the contribution of these stable components, assuming that the hard, variable component does not change the spectral shape with CR[4–9], based on no apparent correlation of SR[15–40] to CR[4–9] (Figure 3 of Shrader et al. 2015). We reduce an equal amount of count rates from CR in each band below 4 keV until the linear fit of each SR vs. CR[4–9] plot is flat. The result is shown as the red points in the bottom panels of Figure 4, obtained by reducing the soft CR by 0.213 (SR[0.5–1]), 0.418 (SR[1–2]) and 0.184 (SR[2–4]) cnts  $s^{-1}$ .

Since this approach works apparently well, we re-define 10 energy bands between 0.3–4 keV and measure the reduction amount for each bin in the same way. We use all the XIS (0,1,3) data between 0.5–4 keV and derive the reduction amount for the XIS1 from the count rate ratio. The FI sensors are not sensitive below 0.5 keV, so we only use XIS1 for the 0.3–0.5 keV bin. Their  $1\sigma$  errors are evaluated from the cases when a linear fit to the plot includes a flat solution within a  $1\sigma$  error. Figure 5 shows the stable emission spectrum for XIS1 estimated from this method.

The stable spectrum peaks at  $\sim 0.9$  keV and extends up to  $\sim 4$  keV. If this spectrum originates from optically thin thermal plasma emission, these profiles require, at least two temperature components at  $kT \sim 0.9$  keV and  $\gtrsim 3$  keV. These temperatures are similar to the  $T_2$  ( $kT \sim 0.6$  keV) and  $T_3$  ( $kT \sim 4$  keV) components in the *XMM-Newton* observations in 2010 (Smith et al. 2012). In fact, the sum of the three cooler components in the best-fit *XMM/OBS1* spectrum ( $T_1$ :  $kT \sim 0.11$  keV,  $T_2$  and  $T_3$ )<sup>2</sup> fits nicely to this stable spectrum by multiplying the model normalization by 0.64 (Figure 5). This result suggests that the stable spectrum has the same origin as the  $T_2$  and  $T_3$  components. The difference in normalization may be due to time variation or the different measurement method — we estimate the stable spectrum from the broad-band color variation, while Smith et al. (2012) estimated these cool components from emission lines in the time averaged high resolution spectra. The minor  $T_1$  component might also be a part of this stable emission, but we cannot judge it conclusively from the *Suzaku* data.

### 3.3. Phase Resolved Spectra

To understand the nature of the softness dips, we extract XIS spectra during each dip, which is defined as the interval between the middle points of the fall and rise in the best-fit SR[0.5–1] model (i.e.,  $[t_c^i - (T_{fb}^i + T_{tr}^i)/2, t_c^i + (T_{fb}^i + T_{tr}^i)/2]$ ). We also extract XIS spectra of the baseline interval. The FI (XIS0 and 3) spectra of each interval are combined. The XIS1 spectra of the baseline interval, all the softness dips, and the stable emission are overlaid in the left panel of Figure 6. The baseline and softness dip spectra have a factor of  $\lesssim 2$  flux variations in both the soft and hard bands. In the right panel of Figure 6, we show the XIS1 spectra of the baseline interval and the softness dips, normalized with the normalization parameter of the variable thermal component to the baseline spectrum. The softness dip spectra clearly have stronger soft-band cut-offs than the baseline spectrum, but they do not show significant changes in the hard band slope or the flux ratio of the hydrogen-like and helium-like iron  $K$  emission lines. This plot further supports our conclusion that the softness dips are produced by changes in the absorption, and not the plasma temperature.

We then fit all these spectra simultaneously. For the stable emission, we assume an absorbed two-temperature thermal model — (apec + apec)TBabs. For the hard variable emission, we apply a one-temperature thermal (apec) model plus two Gaussian lines at 6.4 keV and 7.04 keV for iron  $K_\alpha$  and  $K_\beta$  fluorescence, suffering common absorption.<sup>3</sup> We tie all the thermal emission parameters except for the normalizations. We vary the normalization of the fluorescent iron  $K_\alpha$  line and tie the normalization of the fluorescent iron  $K_\beta$  line to 12% of this value.

We first try simple absorption (TBabs, Wilms et al. 2000) for the variable component. The spectra above 0.8 keV fit well, but the softness dip spectra below 0.8 keV show significant deviations with a bad chi-square value (reduced  $\chi^2 = 1.50$ , dof = 2214, see the residual in the bottom panel of Figure 7). This looks as if less absorbed emission emerges during each softness dip interval. Since the stable emission is constrained, this emission should be a part of the variable component, which is not absorbed during the softness dip event, so the absorption is partial. We therefore apply a

<sup>2</sup> The  $EM_2$  value is reduced by an order of magnitude from the value in Table 4 of Smith et al. (2012), to correct the typographical error of the exponent of the unit (R. Lopes de Oliveira, private comm.).

<sup>3</sup> Smith et al. (2012) suggested the presence of an extremely embedded hard thermal component. We consider it as Compton reflection of the hard variable thermal emission, which should be accompanied by fluorescent iron emission lines. Our preliminary fit to the *Suzaku* spectra suggest negligible contribution of this component, possibly due to different geometry of the X-ray emitting source and the cold matter or reflector (Morihana et al. 2014). We, therefore, do not include this component in our model.

partial covering model, `pcfabs`, for each softness dip, in addition to simple absorption common for all spectra, which is required for absorption to the baseline spectra. Then, the deviation decreases substantially (reduced  $\chi^2 = 1.35$ , d.o.f. = 2208, Table 2 and the top and middle panels of Figure 7). In summary, the applied model to each spectrum  $F_{X,i}$  ( $i$ : baseline, 1–6) is:

$$F_{X,i} = F_X[V_i] + F_X[S] \quad (5)$$

$$F_X[V_i] = (\text{apec}\{kT[V], Z[V], EM[V_i]\} + \text{gauss}_{6,40}\{F_{X,\text{FeIK}\alpha}[V_i]\} + \text{gauss}_{7,04}\{0.12F_{X,\text{FeIK}\alpha}[V_i]\}) \\ \text{pcfabs}\{N_{\text{H,PC}}[V_i], CF_{\text{PC}}[V_i]\} * \text{TBabs}\{N_{\text{H}}[V]\} \quad (6)$$

$$F_X[S] = (\text{apec}\{kT[S_C], EM[S_C]\} + \text{apec}\{kT[S_H], EM[S_H]\})\text{TBabs}\{N_{\text{H}}[S]\} \quad (7)$$

where square brackets show the emission component —  $V_{(i)}$ : ( $i$ -th) variable component,  $S_{(C/H)}$ : (cool/hot) stable component — and curly brackets show free parameters for each spectral component. The spectral parameters with the subscript  $i$  are fitted independently between the spectra, while the others are tied between them. The best-fit plasma temperature of the variable component is  $kT \sim 12.2$  keV, typical of  $\gamma$  Cas. The absorption columns of the partial absorbers are between  $2.4\text{--}8.1 \times 10^{21}$   $\text{cm}^{-2}$ , while the covering fractions are localized in two ranges,  $\sim 40\%$  and  $\sim 70\%$ . The common absorption, representing the  $N_{\text{H}}$  to the baseline spectra, is very low at  $\sim 3.8 \times 10^{20}$   $\text{cm}^{-2}$  and close to the column density to the Be star measured from the UV spectroscopy ( $1.45 \pm 0.3 \times 10^{20}$   $\text{cm}^{-2}$ , Jenkins 2009). There is little local absorption outside of the softness dip intervals. The equivalent width of the fluorescent iron  $K_{\alpha}$  line does not vary significantly at  $\sim 60$  eV, suggesting that the softness dip absorbers are not responsible for the iron fluorescence emission.

### 3.4. Pulse Search for Data above 2 keV

Earlier pulsation analysis with the *XMM-Newton* data was performed for the broad 0.8–10 keV band (Lopes de Oliveira et al. 2010; Smith et al. 2012). Since soft X-ray emission from  $\gamma$  Cas is affected by the dip events, we undertake a new pulse search only above 2 keV using the standard Fourier analysis. However, we find no significant pulse in our analysis, either.

## 4. DISCUSSION

We find that hard, variable X-ray emission from  $\gamma$  Cas is frequently occulted by absorbers with  $\log N_{\text{H}} \sim 21\text{--}22$   $\text{cm}^{-2}$  on timescales of a kilo-second or longer during the *Suzaku* observation. Earlier *XMM-Newton* observations of  $\gamma$  Cas also reported similar variations in the hardness ratio (Lopes de Oliveira et al. 2010; Smith et al. 2012). Gamma Cas and HD 110432, a  $\gamma$  Cas analogue, show changes in time-averaged X-ray absorption between observations (e.g., Figure 3 in Smith et al. 2016), which are perhaps caused by variations in numbers and column densities of softness dip absorbers for each observation. Rapidly changing X-ray absorbers are probably a common feature in  $\gamma$  Cas analogues.

All softness dips are symmetrical. This can be explained if, in each softness dip event, a blob-like absorber passes over a discrete X-ray emitting region with a constant projection velocity. The triangular dips 2, 3 and 5 can be produced by absorbers that block only a part of an X-ray emitting region. The trapezoidal dips 1, 4 and 6 can be produced in the following three cases. In the first case, an absorber moves over an X-ray emitting region in such a way that its covering factor is constant during the flat bottom, but this situation seems unlikely to occur. In the second case, an absorber is fully inside of a larger X-ray emitting region on projection during the flat bottom. In this case,  $T_{\text{tr}}$  relates to the projection size of the absorber, while  $T_{\text{fb}}$  corresponds to the travel length of the absorber over the X-ray emitting region, i.e., the minimum size of the X-ray emitting region. The size ratios of the X-ray emitting region over the absorber ( $T_{\text{fb}}/T_{\text{tr}}$ ) are  $\gtrsim 45, 2.4, 7$  for softness dips 1, 4 and 6. Assuming two-dimensional symmetry on the projection surface, the areal ratios are  $\gtrsim 2000, 5, \text{ and } 50$ . In this case, the covering factors of the partial covering absorbers are  $\lesssim 0.05, 17$  and  $1.8\%$ , which contradict those measured from the spectral fits,  $\sim 41, 65, \text{ and } 35\%$ . In the third case, an absorber is larger than an X-ray emitting region and fully obscures it during the flat bottom. In this case,  $T_{\text{tr}}$  relates to the projection size of the X-ray emitting region, and  $T_{\text{fb}}$  corresponds to the absorber size. The covering factor of the absorber to this X-ray emitting region becomes unity, so there should be other uncovered discrete X-ray emitting regions that produce the flat-bottom emission. We conclude that the third case — multiple X-ray emitting regions, one of which is fully covered during each flat bottom — should be the only viable solution. Since the covering factor of each dip is  $\gtrsim 40\%$ , the covered X-ray emitting region should be a major X-ray spot.

Based on the above consideration, the length of the X-ray emitting region ( $L_{\text{proj}}$ ) is expressed in terms of the projected velocity of the absorber ( $v_{\text{proj}}$ ) and the transition timescale as  $L_{\text{proj}} \sim v_{\text{proj}}T_{\text{tr}}$ . The SR[0.5–1] fit suggests at least two distinct groups in  $T_{\text{tr}}$  at 0.4–1 ksec and 4–7 ksec. This might suggest two kinds of absorbers with

different projection velocities or two different X-ray emitting regions occulted by the absorbers. On the other hand, the absorber's projection length ( $l_{\text{proj}}$ ) and the line of sight depth ( $l_{\text{d}}$ ) are related to the dip parameters  $T_{\text{fb}}$  and  $N_{\text{H}}$  as  $l_{\text{proj}} \sim v_{\text{proj}} T_{\text{fb}} \sim (T_{\text{fb}}/T_{\text{tr}}) L_{\text{proj}}$  and  $l_{\text{d}} \sim N_{\text{H}}/\rho_{\text{abs}}$  where  $\rho_{\text{abs}}$  is the absorber's density. Their ratio is  $l_{\text{proj}}/l_{\text{d}} \sim \rho_{\text{abs}} v_{\text{proj}} T_{\text{fb}}/N_{\text{H}} \sim \rho_{\text{abs}} L_{\text{proj}} T_{\text{fb}}/(T_{\text{tr}} N_{\text{H}})$ . The value  $T_{\text{fb}}/(T_{\text{tr}} N_{\text{H}})$  ranges by a factor of  $\gtrsim 25$  for dips 1, 4 and 6. If  $\rho_{\text{abs}}$  and  $L_{\text{proj}}$  do not change significantly between the absorbers, the absorber may not be three dimensionally symmetric, i.e.  $l_{\text{proj}} \approx l_{\text{d}}$ .

The best-fit result of the partial covering model suggests two covering factors,  $\sim 0.4$  and  $\sim 0.7$ . This result may not be consistent with the magnetic star-disk dynamo theory, in which X-rays originate from multiple magnetic loops on the Be stellar surface (see [Smith et al. 2016](#)). Assuming that the magnetic loops spread evenly over the Be star surface, a single X-ray absorber should have a size of  $\sim 0.4$  stellar radius ( $\sim 4 R_{\odot}$ ) and move with a projection velocity of up to  $\sim 5000 \text{ km s}^{-1}$ , which are unrealistic for the wind or disk of the Be star. On the other hand, this result seems to fit with the mass-accreting compact star, which has small numbers of discrete X-ray emitting regions. Interestingly, the sum of the two covering factors is close to unity, perhaps suggesting that one of two distinct X-ray emitting regions on the dipole magnetic poles is occulted occasionally. The cessation seen at  $\sim 10^5 \text{ sec}$  is also similar to the flux drops observed in the high mass X-ray binary, Vela X-1, which can be explained from the propeller effect — inhibition of mass accretion due to the change of the ram pressure of the infalling gas ([Kreykenbohm et al. 2008](#)). As described in the introduction, the companion is perhaps not an accreting neutron star since it shows no evidence of either a power-law tail up to 100 keV or pulsations ([Lopes de Oliveira et al. 2010](#); [Smith et al. 2012](#); [Shrader et al. 2015](#), this work), although a recent model argues the existence of neutron stars with such spectral characteristics like those of  $\gamma \text{ Cas}$  ([Postnov K. 2016](#), in preparation). A  $kT \sim 12 \text{ keV}$  thermal plasma cannot be produced by free-fall accretion onto a sub-dwarf with  $\log g \lesssim 6.5$  ([Heber 2009](#)). We, hence, propose that the hard, variable X-ray emission originates from accretion hot spots of a  $\sim 1 M_{\odot}$  WD companion (Figure 8).

The known WD binary systems that fits most of the above characteristics are the intermediate polars (IP); the IPs are composed of a late-type donor star and a weakly magnetized accreting WD ( $B < 10 \text{ MG}$ ) and their X-ray luminosities range up to  $\sim 10^{33} \text{ ergs s}^{-1}$  ([Yuasa et al. 2010](#)). However, they tend to have higher plasma temperatures ( $kT > 20 \text{ keV}$ ) and larger absorption columns ( $\log N_{\text{H}} \sim 22-23 \text{ cm}^{-2}$ ) than  $\gamma \text{ Cas}$ . An exception is EX Hydrae with low  $kT$  ( $\sim 13 \text{ keV}$ ) and  $N_{\text{H}}$  ( $\sim 7 \times 10^{21} \text{ cm}^{-2}$ ), which may be realized with mass accretion on relatively large areas and accretion shocks at a high altitude ( $\approx 0.3-1 R_{\text{WD}}$ , [Allan et al. 1998](#); [Hayashi & Ishida 2014](#)). The X-ray absorption column of  $\gamma \text{ Cas}$  during the baseline interval is an order of magnitude smaller than that of EX Hydrae, possibly suggesting even larger accretion spots. The absence of an X-ray pulses from  $\gamma \text{ Cas}$  can also be explained if the spot on the opposite side from us is large enough that a part of it always appears in our sight.

The accretion spots should be smaller than the diameter of the companion star, i.e.,  $L_{\text{proj}} \lesssim 0.02 R_{\odot}$  for a  $1 M_{\odot}$  WD ([Provencal et al. 1998](#)). The projection velocity of a blob relative to the X-ray emitting source should be  $v_{\text{proj}} \sim L_{\text{proj}}/T_{\text{tr}} \lesssim 20 \text{ km s}^{-1}$  for softness dips 1, 3, 4 and 6. We here consider the following three components in the presumed Be+WD binary system that could work as X-ray absorbers: i) Be stellar wind, ii) Be decretion disk, and iii) WD accretion disk or the accretion flow onto the companion. For case i), the wind velocity is measured at  $\sim 1700 \text{ km s}^{-1}$  ([Henrichs et al. 1983](#); [Smith & Robinson 1999](#)). Since the companion was almost at quadrature during the *Suzaku* observation ( $\phi \sim 0.57$  in the ephemeris in Orbit 1 in [Smith et al. 2012](#)), its projection velocity is  $\sim 1500 \text{ km s}^{-1}$ , which may be too fast for the X-ray absorbers. For case ii), the decretion disk rotates much slower around the primary star, but the separation between the Be star and the  $1 M_{\odot}$  companion is  $\sim 350 R_{\odot}$ , while the Be disk should not extend beyond the Roche lobe radius, which is  $\sim 213 R_{\odot}$  ([Eggleton 1983](#)). Also the Be disk may not be in the line of sight to the companion star. For case iii), the Keplerian motion is  $\sim 40 \text{ km s}^{-1}$  at  $100 R_{\odot}$  from a  $1 M_{\odot}$  companion, and faster at smaller distances. The absorbers should rotate very far from the WD in an orbit oblique to the orbital plane to meet the condition  $v_{\text{proj}} \lesssim 20 \text{ km s}^{-1}$ . All these components are expected to move faster than the estimated velocity range of the blob. We may need to consider another possible absorbing source.

We also compare the X-ray column density measurements of  $\gamma \text{ Cas}$ , both during the softness dips and the baseline interval, to that expected if the X-ray source is indeed at the position of the WD and embedded in the Be wind. For a separation of  $a = 370 R_{\odot}$ , a radius of  $R = 10 R_{\odot}$ , and a  $\beta = 1$  velocity law, i.e.  $v(r) = v_{\infty}(1 - R/r)^{\beta}$ , the column density of a smooth, non-rotating wind to the WD at quadrature (which is independent of the orbital inclination for a circular orbit) is  $N_{\text{H}} = (\dot{M}_{-7}/v_{\infty,8}) 3.1 \times 10^{20} \text{ cm}^{-2}$  where  $\dot{M}_{-7}$  is the mass-loss rate in units of  $10^{-7} M_{\odot} \text{ yr}^{-1}$ , and  $v_{\infty,8}$  is the terminal velocity of the wind  $v_{\infty}$  in units of  $10^8 \text{ cm s}^{-1}$ . Rotation lowers the wind density as a function of the polar angle to the rotation axis  $\theta$  by  $\rho(\theta) \sim \sqrt{1 - \Omega \sin^2(\theta)}$  ([Owocki et al. 1998](#)) where  $\Omega = v_{\text{rot}}^2 R/GM$  is the square of the fraction of the equatorial rotation speed  $v_{\text{rot}}$  to the equatorial Keplerian velocity. As Be stars are rapid rotators,

values of  $\Omega = 0.8 [0.95]$  have densities at the equator that are 0.45 [0.22] lower than the poles, so the quoted  $N_{\text{H}}$  formula above is an upper limit. Alternatively, any gravitational focusing of the wind by the WD (most likely a small effect) and material flowing around the WD (a larger effect) will increase the  $N_{\text{H}}$  values obtained from this calculation. Additionally, the inclusion of clumping can cause  $N_{\text{H}}$  to fluctuate in time by an order of magnitude depending on the clump model (Oskinova et al. 2012), as indeed is shown by this analysis. So ideally the computed  $N_{\text{H}}$  values should be between the baseline interval  $N_{\text{H}} = 3.8 \times 10^{20} \text{ cm}^{-2}$  and the softness dip interval  $N_{\text{H}} = 2.4 - 8.1 \times 10^{21} \text{ cm}^{-2}$ . Plugging in the  $\gamma$  Cas parameters of  $v_{\infty,8} \approx 1.7$  (Henrichs et al. 1983; Smith & Robinson 1999) and mass-loss rates ranging from  $\dot{M}_{-7} \approx 0.1$  (Henrichs et al. 1980) to  $\dot{M}_{-7} \approx 5$  (upper limit in Lamers & Waters 1987, lower value quoted is  $\dot{M}_{-7} \approx 0.25$ ), the expected absorbing column ranges from  $N_{\text{H}} = 0.18 - 9.2 \times 10^{20} \text{ cm}^{-2}$ . This upper limit lies within the softness dip interval and baseline interval values, consistent with the high mass-loss rate found by Lamers & Waters (1987).

In either scenario, some of these absorbers may be trapped by the companion and accreted onto its surface. The absorber mass is expressed as  $M_{\text{abs}} \sim \gamma m_p \rho_{\text{abs}} l_{\text{d}} l_{\text{proj}}^2 \sim \gamma m_p N_{\text{H}} (L_{\text{proj}} T_{\text{fb}} / T_{\text{tr}})^2$  where  $m_p$  is the proton mass and  $\gamma$  is mass fraction with respect to hydrogen (1.39 for solar abundance matter). For softness dip 4,  $M_{\text{abs}} \sim 5 \times 10^{16} \text{ g} \sim 3 \times 10^{-17} M_{\odot}$ . If a blob similar to this size accretes onto the presumed WD companion, the released gravitational energy is  $\sim 10^{34}$  ergs, which is comparable to the X-ray energies of the shot events (Robinson & Smith 2000).

The work suggests stable X-ray emission from two plasma components. The cool component has  $\log L_{\text{X}} / L_{\text{bol}} \sim -7.3$  ( $L_{\text{bol}}$ : bolometric luminosity),  $kT \sim 0.9$  keV and no apparent time variation, which are similar to X-ray emission from OB stars (e.g., Berghöfer et al. 1997). This component perhaps originates from radiatively driven winds from the primary Be star. The hot component has only a factor of 3 higher luminosity,  $\sim 2.0 \times 10^{31} \text{ ergs s}^{-1}$ , than the cool component, but it has a very high plasma temperature at  $kT \sim 5$  keV. It may originate from the head-on collision between the Be disk and the WD wind or the primary wind if the disk is not wind fed.

A WD is the end product of a star with an initial mass of  $\lesssim 10 M_{\odot}$  (see references in Winget & Kepler 2008). A star born with  $\sim 15 M_{\odot}$  should explode as a core-collapse supernova before the companion evolves into a WD. A possible evolutionary channel that produces a Be + WD binary system is binary interaction. At a late evolutionary stage, significant mass of the (current) companion may be stripped off to the (current) primary star through mass transfer. The companion loses mass to drive core nuclear burning and becomes a WD, while the primary star increases its mass to become a Be star. Simulations suggest that binary interaction can produce  $10^5$  Be + WD binary systems in our galaxy (Shao & Li 2014). The gainer is expected to become an outlier among the cluster members in the HR diagram, recognized as a blue straggler (Knigge et al. 2009). Actually, a few  $\gamma$  Cas analogues are classified as blue stragglers (Smith et al. 2016). The rapid rotation and Be disk of  $\gamma$  Cas and its analogues could be an outcome of the mass transfer activity<sup>4</sup>.

Mannucci et al. (2006) suggest two populations in Type Ia supernovae (SNe): one explodes within  $10^8$  yr of their stellar birth and the other with a much wider time range up to  $\sim 3$  Gyr. The  $\gamma$  Cas companion could explode as a “prompt” Type Ia SN if the supposed mass accretion continues. Assuming a WD companion with  $M \sim 1 M_{\odot}$ ,  $r \sim 0.01 R_{\odot}$ , and a 10% conversion efficiency from gravitational energy to X-ray energy, the mass accretion rate is estimated at  $\approx 8 \times 10^{-10} M_{\odot} \text{ yr}^{-1}$ . At this rate, it takes  $\approx 5 \times 10^8$  years to gain  $\sim 0.4 M_{\odot}$  and reach the Chandrasekhar mass limit, which is longer than the lifetime of a  $15 M_{\odot}$  star. The mass accretion rate needs to be actually higher than the above estimate or increase significantly in a later stage if the WD companion is to explode as a “prompt” Type Ia SN.

## 5. CONCLUSION

The *Suzaku* XIS observation of  $\gamma$  Cas in 2011 July detects flux variations on short ( $\lesssim 1$  ksec) and long ( $\gtrsim 10$  ksec) timescales in all of the 0.5–1, 1–2, 2–4 and 4–9 keV bands. These light curves look very similar at a first glance, but they show abrupt color variations, which are recognized as “softness dips” in time series of the softness ratios. These observed variations are typical of  $\gamma$  Cas as earlier X-ray observations detected similar flux and color variations from the star. We identify six softness dip events in time series of the softness ratio of the 0.5–1 keV band over the 4–9 keV band. These dips are recognized more weakly in the softness ratios of the harder energy band and apparently uncorrelated to the 4–9 keV flux variation. This result indicates that the softness dips are produced by sudden increases of X-ray absorption in the line of sight, and not the variation of the plasma temperature.

All six softness dips are symmetrical in time series of the softness ratios and some of them show saturation-like

<sup>4</sup> We, here, do not mention the origin of the rapid rotation and Be disk of the classical Be stars, in general. Meurs et al. (1992) found insignificant difference in X-ray luminosity between the classical Be stars and normal OB stars, and therefore did not suggest the presence of a compact companion for every classical Be star.

flat bottoms. Each softness dip can be reproduced by a symmetrical trapezoidal shape with two transition timescales of 0.4–1 ksec and 4–7 ksec. All spectra during each softness dip interval and outside of the dips (baseline interval) can be reproduced by  $kT \sim 12$  keV plasma emission with iron  $K$  fluorescence. The baseline spectrum suffers almost negligible absorption at  $N_{\text{H}} \sim 3.8 \times 10^{20} \text{ cm}^{-2}$ , which is consistent with the optical extinction. The softness dip spectra need additional absorption of  $N_{\text{H}} \sim 2.4\text{--}8.1 \times 10^{21} \text{ cm}^{-2}$  covered partially by  $\sim 35\text{--}80\%$ . The absorbers are perhaps blobs passing over an X-ray emitting region, which is perhaps one of the magnetically funneled accretion spots of a WD companion orbiting around the Be star.

The softness ratio in each energy band has a weak but significant correlation with the 4–9 keV flux, suggesting the presence of stable, soft X-ray emission. The stable spectrum reproduced from the correlation plots requires two plasma components at  $kT \sim 0.9$  and 5.4 keV with negligible absorption, which probably correspond to the intermediate temperature components found from high resolution grating spectra. The cool component probably originates from the Be primary stellar wind, while the hot component may originate from the head-on collision of either the Be or WD wind with the Be disk.

The formation of a Be + WD binary requires mass transfer between two relatively massive stars. Gamma Cas may have experienced such activity in the past, which might be responsible for the rapid rotation of the Be star and the formation of the Be disk. If significant mass accretes back from the Be star during its lifetime, the WD companion might explode as a prompt Type Ia supernova.

The authors are grateful to the anonymous referee for very useful comments and suggestions that helped to significantly improve the paper. The authors appreciate Drs. Vanbeveren, D., Drake S., Smith, M., Mukai, K., Pottschmidt, K., and Shrader, C. for providing important information and discussion. This research has made use of data obtained from the High Energy Astrophysics Science Archive Research Center (HEASARC), provided by NASA’s Goddard Space Flight Center. This research has made use of NASA’s Astrophysics Data System Bibliographic Services. K.H. is supported by the *Chandra* grant GO4-15019A, the *XMM-Newton* grant NNX15AK62G, and the ADAP grant NNX15AM96G. C.M.P.R. is supported by an appointment to the NASA Postdoctoral Program at the Goddard Space Flight Center, administered by Universities Space Research Association under contract with NASA.

*Facility:* Suzaku (XIS)

## REFERENCES

- Allan, A., Hellier, C., & Beardmore, A. 1998, *MNRAS*, 295, 167
- Arnaud, K. A. 1996, in *Astronomical Society of the Pacific Conference Series*, Vol. 101, *Astronomical Data Analysis Software and Systems V*, ed. G. H. Jacoby & J. Barnes, 17
- Asplund, M., Grevesse, N., Sauval, A. J., & Scott, P. 2009, *ARA&A*, 47, 481
- Berghöfer, T. W., Schmitt, J. H. M. M., Danner, R., & Cassinelli, J. P. 1997, *A&A*, 322, 167
- Eggleton, P. P. 1983, *ApJ*, 268, 368
- Gies, D. R., Bagnuolo, Jr., W. G., Baines, E. K., et al. 2007, *ApJ*, 654, 527
- Harmanec, P., Habuda, P., Štef, S., et al. 2000, *A&A*, 364, L85
- Hayashi, T., & Ishida, M. 2014, *MNRAS*, 441, 3718
- Heber, U. 2009, *ARA&A*, 47, 211
- Henrichs, H. F., Hammerschlag-Hensberge, G., Howarth, I. D., & Barr, P. 1983, *ApJ*, 268, 807
- Henrichs, H. F., Hammerschlag-Hensberge, G., & Lamers, H. J. G. L. M. 1980, in *ESA Special Publication*, Vol. 157, 2nd European IUE Conference, ed. B. Battrock & J. Mort, 147–149
- Horaguchi, T., Kogure, T., Hirata, R., et al. 1994, *PASJ*, 46, 9
- Jenkins, E. B. 2009, *ApJ*, 700, 1299
- Knigge, C., Leigh, N., & Sills, A. 2009, *Nature*, 457, 288
- Kokubun, M., Makishima, K., Takahashi, T., et al. 2007, *PASJ*, 59, 53
- Koyama, K., Tsunemi, H., Dotani, T., et al. 2007, *PASJ*, 59, 23
- Kreykenbohm, I., Wilms, J., Kretschmar, P., et al. 2008, *A&A*, 492, 511
- Kubo, S., Murakami, T., Ishida, M., & Corbet, R. H. D. 1998, *PASJ*, 50, 417
- Lamers, H. J. G. L. M., & Waters, L. B. F. M. 1987, *A&A*, 182, 80
- Lopes de Oliveira, R., Smith, M. A., & Motch, C. 2010, *A&A*, 512, A22
- Mannucci, F., Della Valle, M., & Panagia, N. 2006, *MNRAS*, 370, 773
- Meurs, E. J. A., Pitters, A. J. M., Pols, O. R., et al. 1992, *A&A*, 265, L41
- Mitsuda, K., Bautz, M., Inoue, H., et al. 2007, *PASJ*, 59, 1
- Morihana, K., Tsujimoto, M., & Ishida, M. 2014, in *Suzaku-MAXI 2014: Expanding the Frontiers of the X-ray Universe*, ed. M. Ishida, R. Petre, & K. Mitsuda, 184
- Morrison, R., & McCammon, D. 1983, *ApJ*, 270, 119
- Motch, C., Lopes de Oliveira, R., & Smith, M. A. 2015, *ApJ*, 806, 177
- Murakami, T., Koyama, K., Inoue, H., & Agrawal, P. C. 1986, *ApJL*, 310, L31
- Nemravová, J., Harmanec, P., Koubský, P., et al. 2012, *A&A*, 537, A59
- Oskina, L. M., Feldmeier, A., & Kretschmar, P. 2012, *MNRAS*, 421, 2820
- Owens, A., Oosterbroek, T., Parmar, A. N., et al. 1999, *A&A*, 348, 170
- Owocki, S. P., Gayley, K. G., & Cranmer, S. R. 1998, in *Astronomical Society of the Pacific Conference Series*, Vol. 131, *Properties of Hot Luminous Stars*, ed. I. Howarth, 237

- Parmar, A. N., Israel, G. L., Stella, L., & White, N. E. 1993, *A&A*, 275, 227
- Provencal, J. L., Shipman, H. L., Høg, E., & Thejll, P. 1998, *ApJ*, 494, 759
- Rivinius, T., Carciofi, A. C., & Martayan, C. 2013, *A&A Rv*, 21, 69
- Robinson, R. D., & Smith, M. A. 2000, *ApJ*, 540, 474
- Robinson, R. D., Smith, M. A., & Henry, G. W. 2002, *ApJ*, 575, 435
- Serlemitsos, P. J., Soong, Y., Chan, K.-W., et al. 2007, *PASJ*, 59, 9
- Shao, Y., & Li, X.-D. 2014, *ApJ*, 796, 37
- Shrader, C. R., Hamaguchi, K., Sturmer, S. J., et al. 2015, *ApJ*, 799, 84
- Sigut, T. A. A., & Jones, C. E. 2007, *ApJ*, 668, 481
- Smith, M. A., Cohen, D. H., Gu, M. F., et al. 2004, *ApJ*, 600, 972
- Smith, M. A., Lopes de Oliveira, R., & Motch, C. 2016, *Advances in Space Research*, 58, 782
- Smith, M. A., & Robinson, R. D. 1999, *ApJ*, 517, 866
- Smith, M. A., Robinson, R. D., & Corbet, R. H. D. 1998, *ApJ*, 503, 877
- Smith, M. A., Lopes de Oliveira, R., Motch, C., et al. 2012, *A&A*, 540, A53
- Stee, P., Delaa, O., Monnier, J. D., et al. 2012, *A&A*, 545, A59
- Takahashi, T., Abe, K., Endo, M., et al. 2007, *PASJ*, 59, 35
- Tokovinin, A. A. 1997, *A&AS*, 124, doi:10.1051/aas:1997181
- van Leeuwen, F. 2007, *A&A*, 474, 653
- White, N. E., Swank, J. H., Holt, S. S., & Parmar, A. N. 1982, *ApJ*, 263, 277
- Wilms, J., Allen, A., & McCray, R. 2000, *ApJ*, 542, 914
- Winget, D. E., & Kepler, S. O. 2008, *ARA&A*, 46, 157
- Yuasa, T., Nakazawa, K., Makishima, K., et al. 2010, *A&A*, 520, A25

**Table 1.** Softness Dip Parameters

$i$	1	2	3 <sup>†0</sup>	4	5	6
Softness Dip						
$t_c^i$ (ksec)	$\leq 13.4 \pm 0.5^{\dagger 1}$	$56.1 \pm 0.4$	$65.1 \pm 0.1$	$72.7 \pm 0.2$	$81.7 \pm 0.5$	$\geq 109.4 \pm 0.8^{\dagger 1}$
$T_{fb}^i$ (ksec)	$\geq 22.5 \pm 1.0^{\dagger 1}$	$0.0 \pm 2.2$	$0.0 \pm 0.1$	$2.4 \pm 0.7$	$0.1 \pm 3.3$	$\geq 7.4 \pm 1.7^{\dagger 1}$
$T_{tr}^i$ (ksec)	$0.5 \pm 0.5$	$7.5 \pm 1.4$	$1.1 \pm 0.1$	$1.0 \pm 0.7$	$4.0 \pm 1.4$	$1.2 \pm 3.8$
$SR_d^i$	$0.18 \pm 0.01$	$0.22 \pm 0.03$	$0.35 \pm 0.03$	$0.33 \pm 0.02$	$0.16 \pm 0.09$	$0.11 \pm 0.02$
Baseline						
$SR_{bl}$	$0.61 \pm 0.01$					

NOTE— The errors denote  $1\sigma$  confidence ranges. †0: The other parameters are fixed in their error estimates. †1: These values and errors are derived assuming that softness dip 1 (6) falls (recovers) at the start (end) of the observation. Since the softness dip starts (ends) before (after) the observation, only these limits can be placed.

**Table 2.** Simultaneous Fit of the Softness Dip Spectra

	Baseline	1	2	3	4	5	6
Variable Emission							
$kT[V]$ (keV)				$12.1^{+0.3}_{-0.1}$			
$Z[V]$ (solar)				$0.32 \pm 0.02$			
$EM[V_i]$ ( $10^{55} \text{ cm}^{-3}$ )		$3.1 \pm 0.03$	$4.9 \pm 0.04$	$4.1 \pm 0.05$	$3.8 \pm 0.13$	$3.5 \pm 0.05$	$3.2 \pm 0.06$
$F_{X, \text{FeI}K\alpha}[V_i]$ ( $10^{-5} \text{ ph cm}^{-2} \text{ s}^{-1}$ )		$5.3 \pm 0.9$	$7.7 \pm 1.5$	$10.7 \pm 2.6$	$0.0^{+12}$	$6.5 \pm 2.4$	$3.6 \pm 3.1$
$EW_{\text{FeI}K\alpha}[V_i]$ (eV)		$57 \pm 9$	$53 \pm 10$	$87 \pm 21$	$0^{+105}$	$60 \pm 23$	$37 \pm 33$
$N_{\text{H}, \text{PC}}[V_i]$ ( $10^{21} \text{ cm}^{-2}$ )		...	$5.3^{+0.8}_{-0.7}$	$4.9^{+1.2}_{-1.1}$	$5.3^{+1.6}_{-1.4}$	$7.6^{+0.9}_{-0.8}$	$1.8^{+1.9}_{-1.2}$
$CF_{\text{PC}}[V_i]$ (%)		...	$41 \pm 3$	$44^{+6}_{-5}$	$80^{+13}_{-10}$	$65 \pm 3$	$45^{+54}_{-17}$
$N_{\text{H}}[V]$ ( $10^{21} \text{ cm}^{-2}$ )				$0.38^{+0.04}_{-0.06}$			
$F_X$ ( $10^{-10} \text{ ergs cm}^{-2} \text{ s}^{-1}$ )		1.2	1.8	1.5	1.3	1.2	1.2
$L_X$ ( $10^{32} \text{ ergs s}^{-1}$ )		5.3	8.3	7.0	6.5	6.0	5.4
Stable Emission							
$kT[S_C]/kT[S_H]$ (keV)				$0.96^{+0.03}_{-0.04}/5.4_{-1.2}$			
$EM[S_C]/EM[S_H]$ ( $10^{54} \text{ cm}^{-3}$ )				$0.29^{+0.05}_{-0.03}/1.1^{+0.05}_{-0.28}$			
$N_{\text{H}}[S]$ ( $10^{21} \text{ cm}^{-2}$ )				$0.06^{+0.77}$			
$F_X[S_C]/F_X[S_H]$ ( $10^{-12} \text{ ergs cm}^{-2} \text{ s}^{-1}$ )				1.5/4.8			
$L_X[S_C]/L_X[S_H]$ ( $10^{31} \text{ ergs s}^{-1}$ )				0.63/2.0			
Reduced $\chi^2$ (dof)	1.35 (2208)						

NOTE— The errors denote 90% confidence ranges. EW: Equivalent Width.  $CF_{\text{PC}}$ : Covering Fraction.  $V_{(i)}$ : ( $i$ -th) variable component.  $S_{(C/H)}$ : (cool/hot) stable component. The abundances of the stable emission components are fixed at 1 solar value.  $F_X$ : observed flux between 0.3–10 keV.  $L_X$ : absorption corrected intrinsic luminosity between 0.3–10 keV. The distance is assumed at 188 pc.

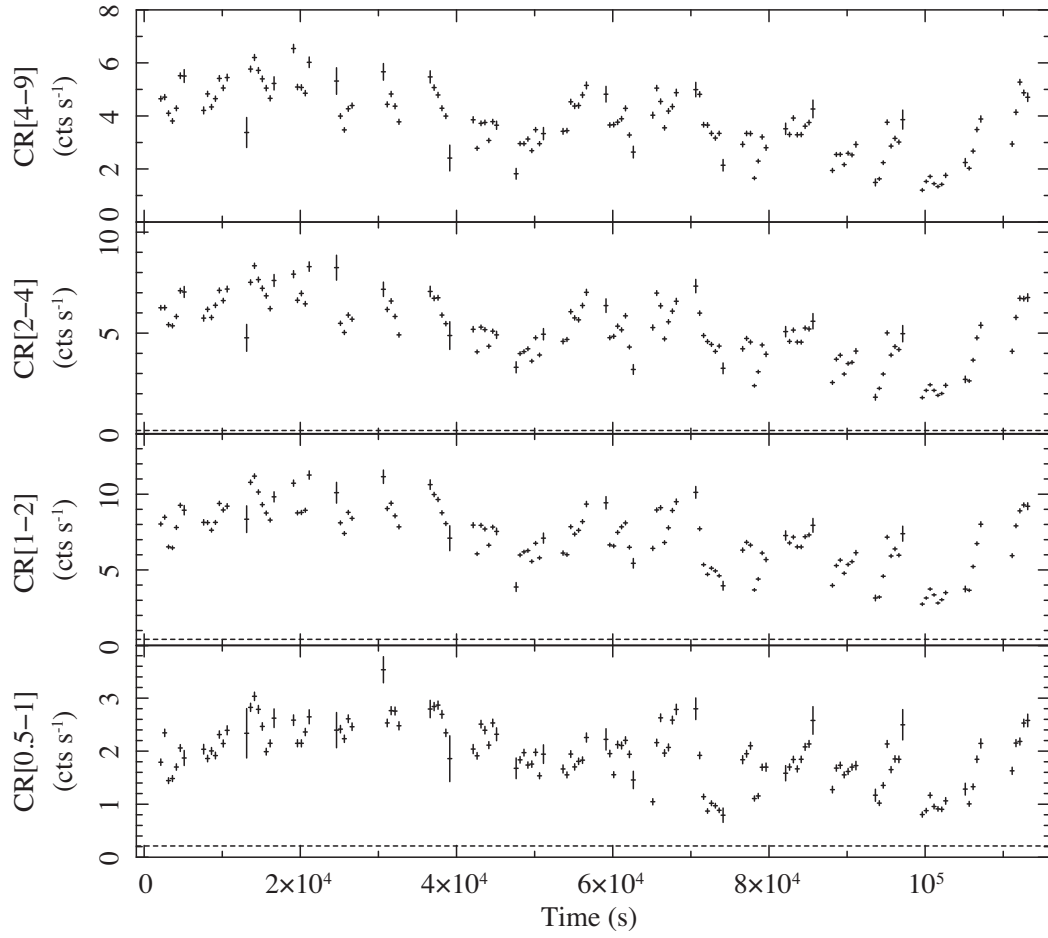


**Figure 1.** XIS0+1+3 light curves of  $\gamma$  Cas in the 4–9 keV (*top*), 2–4 keV (*2nd*), 1–2 keV (*3rd*), and 0.5–1 keV (*bottom*) bands. Each bin has 500 sec. The time origin is at 55755.0 day in Modified Julian Date. The dotted lines show the count rates of the stable emission estimated from the SR vs CR[4–9] plots (Section 3.2, Figure 4).

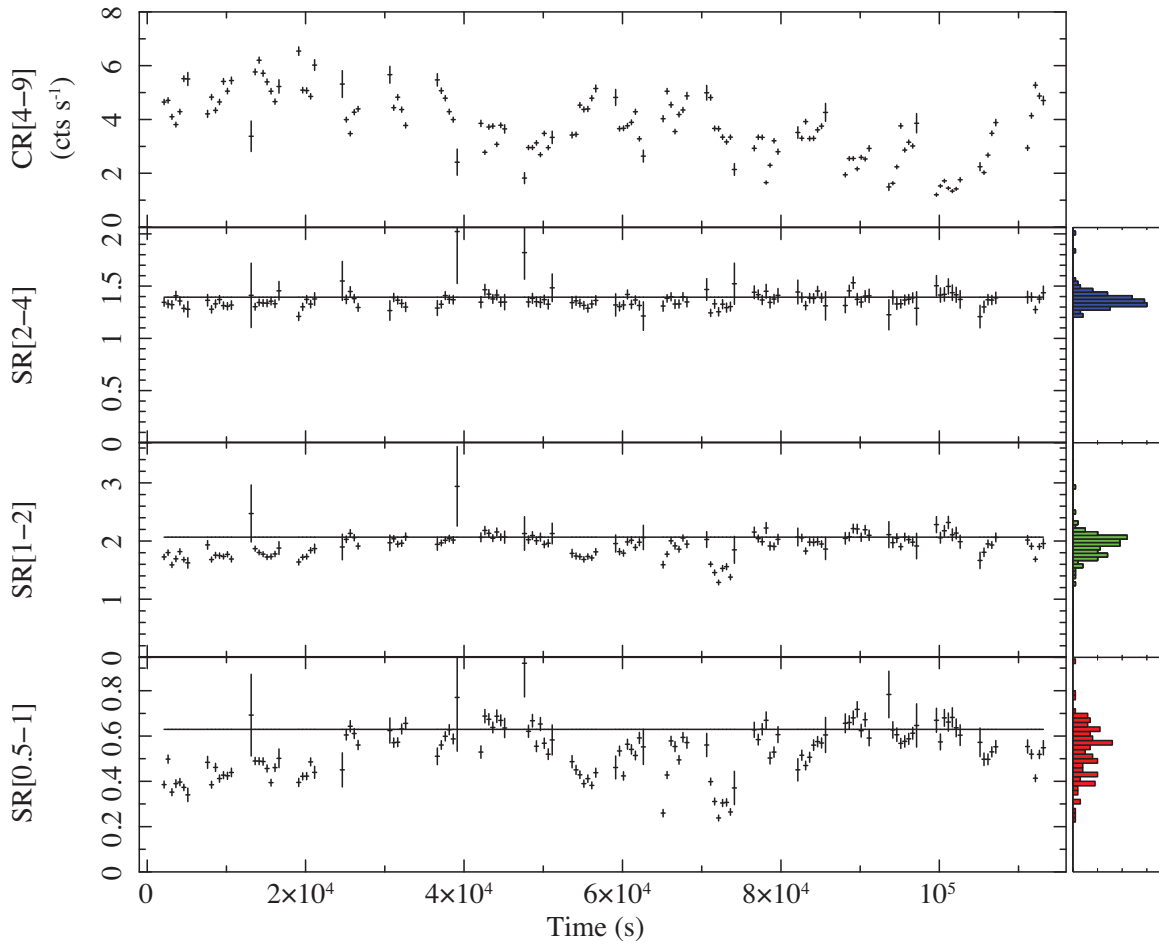


**Figure 2.** XIS0+1+3 light curve in the 4–9 keV band (*top left*, the same as the *top* panel in Figure 1), time series of the softness ratios (*2nd left*: SR[2–4], *3rd left*: SR[1–2], *4th left*: SR[0.5–1]) and distribution histograms of the softness ratios (*right*). The horizontal bars in the 2nd, 3rd and 4th panels show average SRs during the baseline interval.

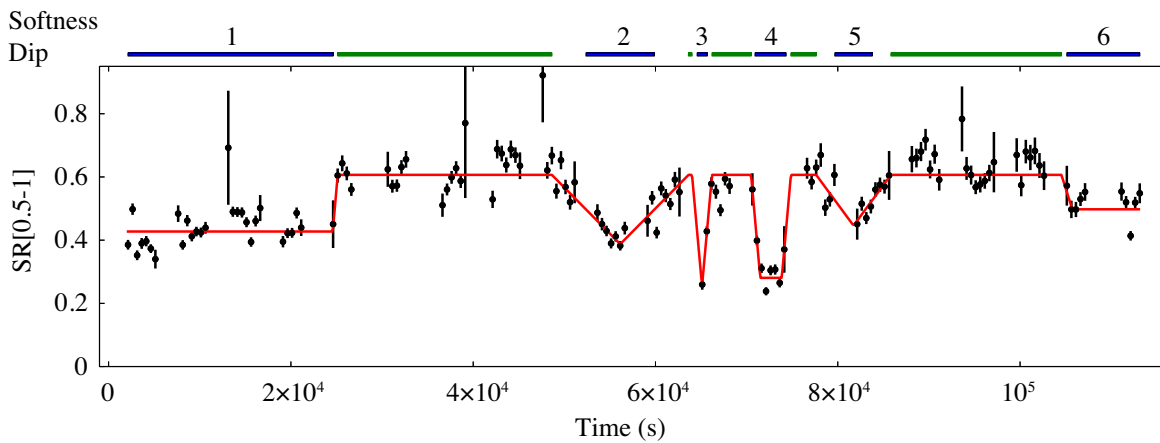


**Figure 3.** SR[0.5–1] fitted by the empirical softness dip model (*solid red line*). Each softness dip interval employed for the spectral analysis is shown as a horizontal bar, while the baseline interval is shown as green bars.

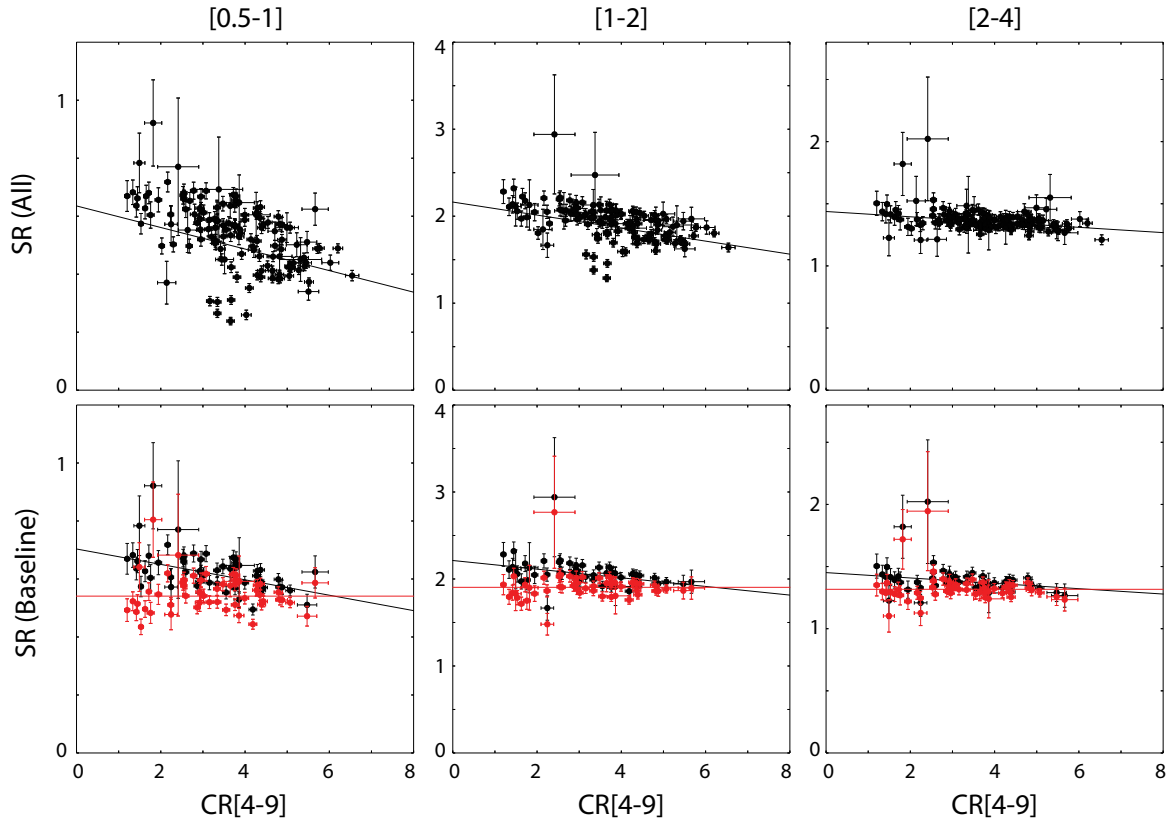


**Figure 4.** The softness ratios (*left*:  $SR[0.5-1]$ , *middle*:  $SR[1-2]$ , *right*:  $SR[2-4]$ ) against the 4–9 keV flux ( $CR[4-9]$ ) for all data points (*top*) and data points obtained during the baseline interval (*bottom*). The *bottom* panels show both the original SRs (*black*) and the SRs after the soft CR reduction thought to be due to the soft, stable component (*red*). Each solid line shows the best linear fit to the corresponding data points.

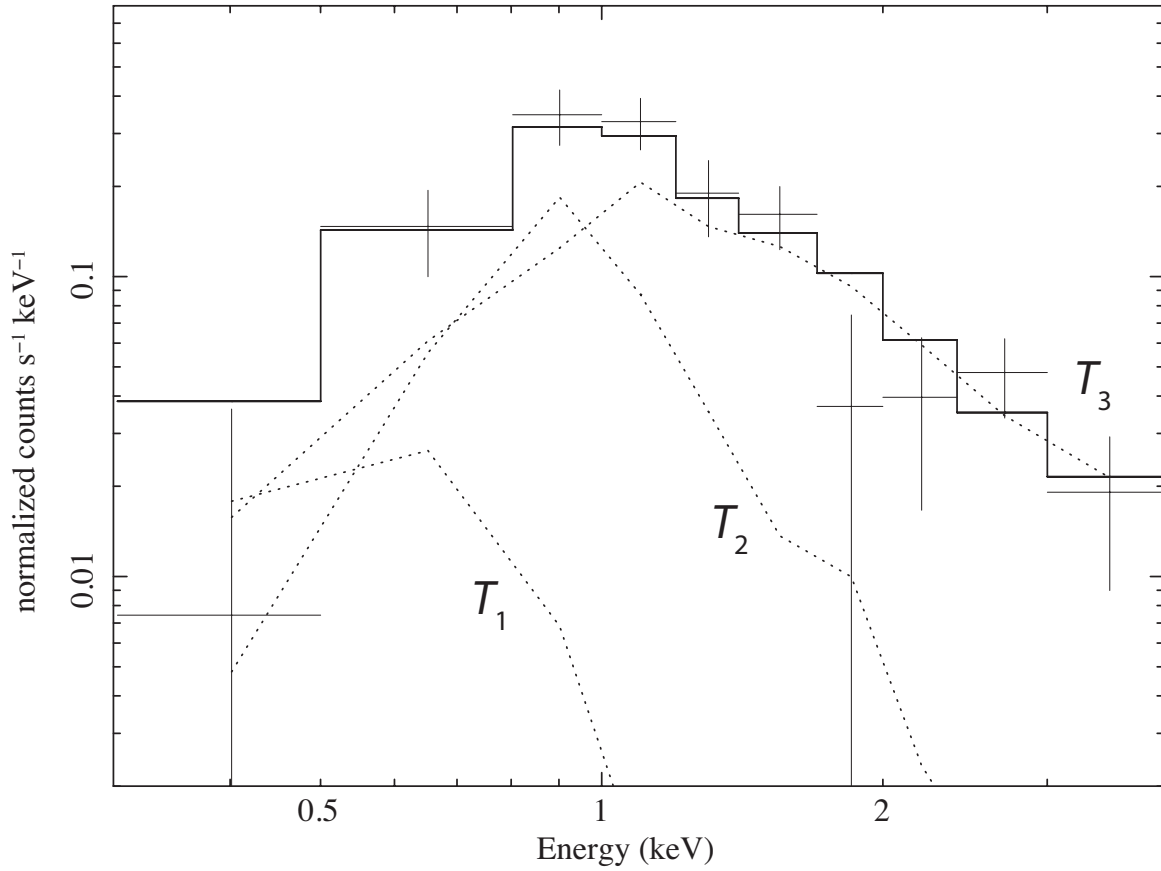


**Figure 5.** Stable emission spectrum for the XIS1, estimated from the SR vs. CR[4–9] plots. The solid line shows the sum of the  $T_1$ ,  $T_2$  and  $T_3$  components of the best-fit OBS1 spectrum in [Smith et al. \(2012\)](#), normalized by 0.64 to fit the *Suzaku* spectrum. The dotted lines show the normalized individual components.

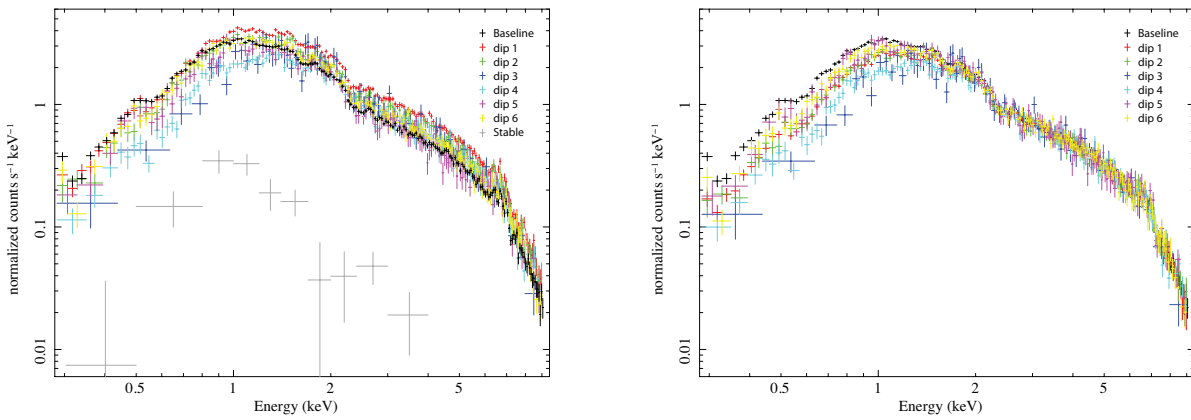


**Figure 6.** *Left:* XIS1 spectra of the baseline interval, all of the softness dips and the stable emission. *Right:* The same spectra, normalized with the best-fit normalization values of the hard variable component.

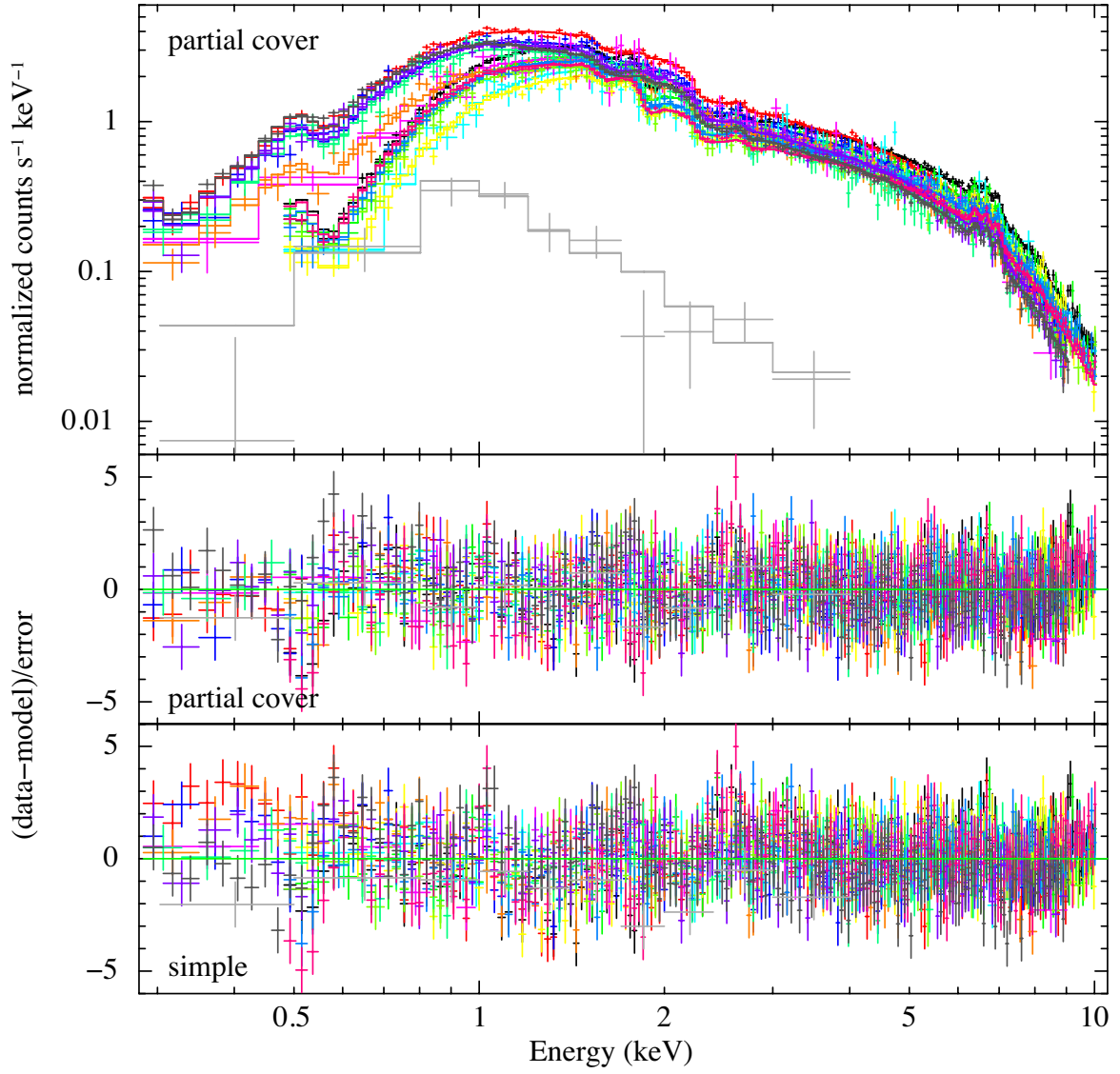


**Figure 7.** FI (XIS0+3) and XIS1 spectra of the baseline interval, all of the softness dips and the stable emission along with their best-fit model in the solid lines, assuming partial covering absorbers (*top*). The figure also shows the residuals to the best-fit models assuming the partial covering absorbers (*middle*) and simple absorbers (*bottom*). The model with the partial covering absorbers has smaller residuals below  $\sim 0.8$  keV.

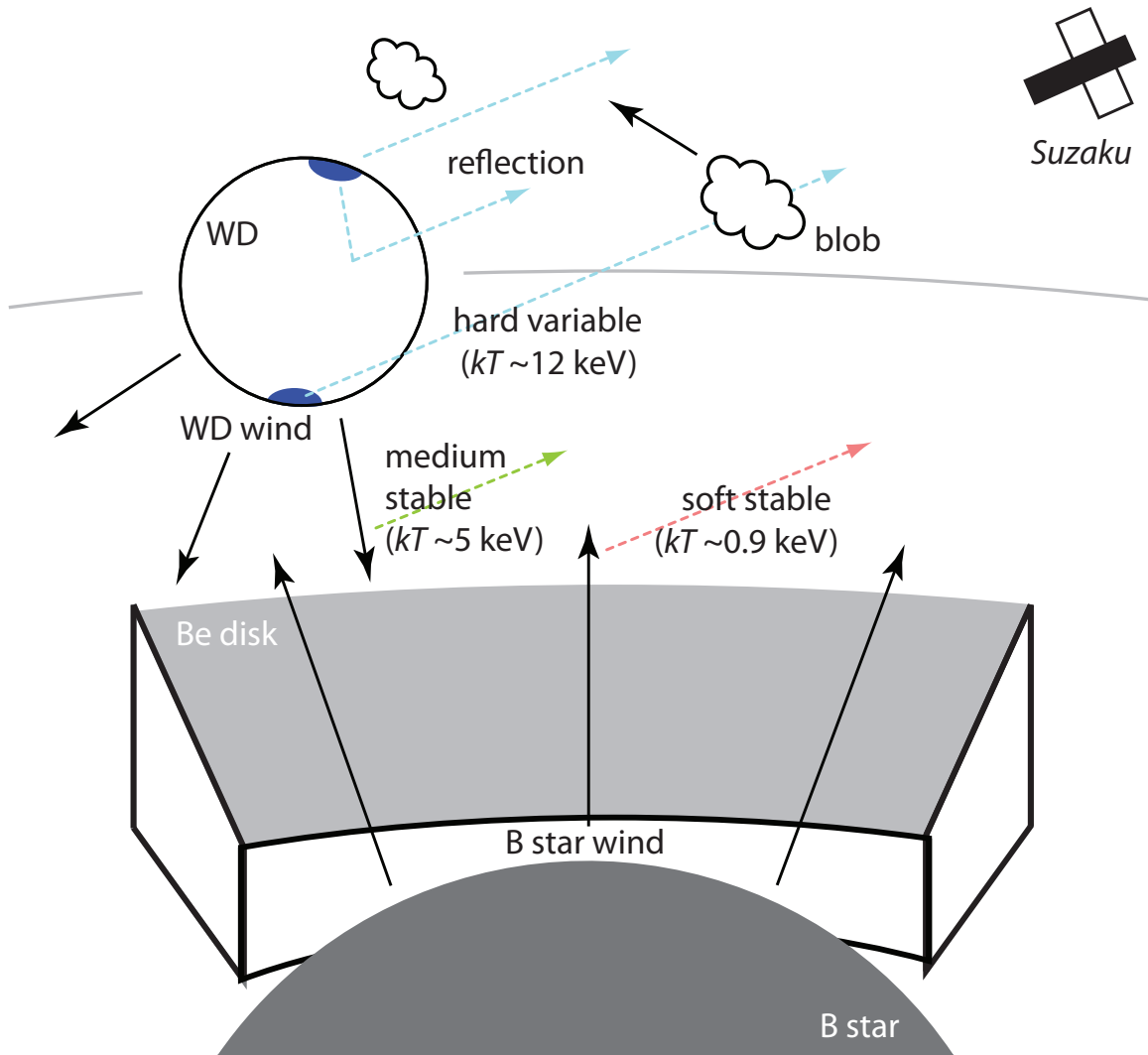


**Figure 8.** Possible geometry of the X-ray emitting and absorbing components.